SPE 59438

Development and Application of Underground Gas Storage Simulator

Masanori Kurihara, SPE, and Jialing Liang, Japan Oil Engineering Co., Ltd., Fujio Fujimoto, Japan National Oil Corporation, Long X. Nghiem, SPE, and Peter Sammon, SPE, Computer Modelling Group, Ltd.

This paper was prepared for presentation at the 2000 SPE Asia Pacific Conference on Integrated Modelling for Asset Management held in Yokohama, Japan, 25–26 April 2000.

Abstract

Japan National Oil Corporation (JNOC) is conducting a survey on underground gas storage (UGS) using inert gas as cushion gas, which makes good use of assets of depleted gas or gas condensate reservoirs. Since the Japanese regulation for a heating value of city gas is extremely strict, a heating value and hence composition of gas withdrawn from those reservoirs must be carefully predicted to successfully design UGS projects.

JNOC has developed an UGS simulator, which can rigorously evaluate a heating value of withdrawn gas taking into consideration all the major phenomena that possibly affect composition of producing gas.

A conventional cubic equation of state (EOS) based 3-D compositional simulator and a PVT simulator were improved to construct the UGS simulator equipped with the functions for calculating physical phenomena; a) molecular diffusion and velocity dependent dispersion, b) three-phase flash including dissolution of gaseous components into water and vaporization of water, c) adsorption of gaseous components onto a rock surface and d) turbulence and Klinkenberg effects. In addition, new functions of MPFA (Multi-Point Flux Approximation) and TVD (Total Variation Diminishing) scheme with local grid refinement in a corner point geometry were incorporated into the simulator to rigorously calculate a fluid flux with permeability tensor and to reduce numerical dispersion, respectively. Furthermore, functions to calculate temperature distributions both in a reservoir and wellbore were added to examine the effect of cooling caused by gas injection and adiabatic expansion on fluid flow and gas composition.

Each function newly developed for the UGS simulator was then validated through test runs using laboratory test data. Field scale simulations for hypothetical reservoirs were also conducted to confirm the simulator's performance as well as to examine the effect of cushion gas volume, working gas volume, reservoir heterogeneity and in situ gas composition on withdrawn gas composition.

This paper describes the development and validation of the UGS simulator followed by the results of field scale simulation runs.

Introduction

Since natural gas was first stored underground in 1915, an increasing number of fields have been utilized for UGS for the purpose of peak shaving and stable energy supply. According to 1991/1992 statistics, there are 550 UGS fields in the world, 425 of which utilizes depleted gas or oil reservoirs [1].

A conventional black oil type simulator or modified black oil type simulator that enables distinction between injection and in situ gas phases has been most commonly used for evaluation/prediction of UGS reservoir performances [2, 3, 4]. A black oil type simulator, however, is not satisfactory to rigorously calculate a heating value and hence composition of withdrawn gas. Major phenomena that possibly affect composition of withdrawn gas are:

- mixing between in situ fluids and injection gas,
- diffusion/dispersion of cushion gas when inert gas is used as cushion gas,
- dissolution of gaseous components into water phase and water vaporization into gas phase,
- adsorption/desorption of gaseous components onto a reservoir rock surface,
- turbulent flow caused by high rate withdrawal/injection and Klinkenberg effect,
- hysteresis of gas-liquid capillary pressure and relative permeability, and
- reservoir temperature change that results from cooling by injecting vaporized LNG and adiabatic expansion of gas.

In addition, numerical errors such as numerical dispersion and discretization errors should be minimized for accurately reproducing these physical phenomena.

There exist several numerical simulators including commercial compositional simulators that can deal with some of these phenomena [4]. None of them, however, are equipped with all the functions required in UGS calculation.

We developed a compositional type UGS simulator incorporating all the functions described above.

Development of UGS Simulator

Base Simulator

The EOS based 3-D, 3-phase, multi-component flow simulator and the PVT simulator, which are the products of Computer Modelling Group Ltd. (CMG), were selected as the base of the UGS simulator because of their credibility for EOS based formulation and numerical solution. The flow simulator calculates phase behavior using cubic EOS of three parameter Peng-Robinson and Soave-Redlich-Kwong with a phase stability test. It also solves single/double permeability type flow equations for orthogonal, cylindrical and corner point grid systems with formulation by IMPECS, AI and FI methods. The flow simulator already has the function to handle the hysteresis of relative permeability. The PVT simulator prepares thermodynamic properties of each component for the flow simulator through regression between calculated and measured PVT properties.

In addition to these two simulators, input/output processors developed by CMG are integrated to construct the UGS simulator. Those programs enable graphical and interactive input and output processing.

Incorporation of New Functions

The base simulator was then improved by adding the functions for calculating physical phenomena; a) molecular diffusion and velocity dependent dispersion, b) three-phase flash including a dissolution of gaseous components into water and vaporization of water, c) adsorption of gaseous components onto a rock surface and d) turbulence and Klinkenberg effects. New functions, MPFA for rigorous calculation of fluid flux with permeability tensor and TVD scheme to reduce numerical dispersion, were incorporated into the UGS simulator to improve numerical solution. Furthermore, functions to calculate the temperature distribution both in a reservoir and wellbore were included.

Fig. 1 illustrates the configuration of the UGS simulator thus constructed. In the case of the single porosity type flow, the updated UGS simulator solves the following system of equations for 3-phase, n_c -component system to obtain $4n_c+3$ primary unknowns, p, T, $N_1,\ldots,N_{n_c}$, ln $K_1^g,\ldots,\ln K_{n_c}^g$, F_g^*, $N_1^w,\ldots,N_{n_c}^w$, $N_{a1},\ldots,N_{an_c}$.

<u>Component flow equations</u>

$$\begin{aligned}&\nabla\bullet\left[\frac{\vec{\vec{k}}k_r^o}{\mu^o}\rho^o x_i\nabla\left(p-\gamma^o d\right)\right]\\&+\nabla\bullet\left[\frac{\vec{\vec{k}}k_r^g}{\mu^g}\rho^g y_i\nabla\left(p+P_c^{og}-\gamma^g d\right)\right]\\&+\nabla\bullet\left[\frac{\vec{\vec{k}}k_r^w}{\mu^w}\rho^w w_i\nabla\left(p-P_c^{ow}-\gamma^w d\right)\right]\\&+\nabla\bullet\vec{J}_i+\tilde{q}_i-\frac{\partial N_i}{\partial t}=0,\qquad i=1,2,\cdots,n_c\end{aligned}\tag{1}$$

<u>Energy conservation equation</u>

$$\begin{aligned}&\nabla\bullet\left[H^o\frac{\vec{\vec{k}}k_r^o}{\mu_o}\rho^o\nabla\left(p-\gamma^o d\right)\right]\\&+\nabla\bullet\left[H^g\frac{\vec{\vec{k}}k_r^g}{\mu_g}\rho^g\nabla\left(p+P_c^{og}-\gamma^g d\right)\right]\\&+\nabla\bullet\left[H^w\frac{\vec{\vec{k}}k_r^w}{\mu_w}\rho^w\nabla\left(p-P_c^{ow}-\gamma^w d\right)\right]\\&+\nabla\bullet\left(\kappa\nabla T\right)+\tilde{Q}_{loss}+\sum_{k=g,o,w}H^k\tilde{q}^k\\&-\frac{\partial}{\partial t}\left[\phi\sum_{k=g,o,w}\left(\rho^k S^k U^k\right)\right]-\frac{\partial}{\partial t}\left[\left(1-\phi\right)c_R\left(T-T_0\right)\right]=0\end{aligned}\tag{2}$$

<u>Volume constraint equation</u>

$$\sum_{k=g,o,w}\left(\frac{N^k}{\rho^k}\right)-\phi=0\tag{3}$$

<u>Phase equilibrium equations</u>

$$\ln\left(K_i^g\right)+\ln\left(\varphi_i^g\right)-\ln\left(\varphi_i^o\right)=0,\quad i=1,2,\cdots,n_c\tag{4}$$

$$\sum_{j=1}^{n_c}\frac{\left(K_j^g-1\right)z_j^*}{1+K_j^g\left(F_g^*-1\right)}=0,\tag{5}$$

where

$$z_i^*=\frac{N_i-N_i^w-N_{ai}}{\sum_{j=1}^{n_c}\left(N_j-N_j^w-N_{aj}\right)}$$

$$N_i^w-w_i\sum_{j=1}^{n_c}N_j^w=0,\quad i=1,2,\cdots,n_c\text{ -1}\tag{6}$$

$$N_w-N_w^w-x_wN^o-y_wN^g=0\tag{7}$$

Adsorption equations

$$N_{ai} = \omega_i \, (1-\phi) \, \rho_R \,, \quad i = 1,\ldots,n_c \qquad (8)$$

Note that Eqs. (6) and (7) are developed for the modular implementation of three-phase calculation utilizing the existing gas-oil flash calculation routines.

The implementations of major calculation functions are described below in more detail.

Molecular diffusion and convective dispersion. To reproduce mixing between cushion gas and injection gas or between in situ gas and injection gas, the simulator has the function to calculate molecular diffusion and two types of convective dispersion, longitudinal and transverse dispersion.

The dispersive flux vector of component i through gas and oil phases, $\vec{J}_i$ in Eq. (1), is given by

$$\vec{J}_i = -\sum_{k=g,o} \phi \rho^k S^k \vec{\vec{D}}_i^k \nabla x_i^k \,, \quad i = 1,\ldots,n_c \,. \qquad (9)$$

The total dispersion tensor, $\vec{\vec{D}}_i^k$, which consists of isotropic molecular diffusion and convective dispersion, is expressed as [5]

$$\vec{\vec{D}}_i^k = \begin{bmatrix} D_{i,xx}^k & D_{i,xy}^k & D_{i,xz}^k \\ D_{i,yx}^k & D_{i,yy}^k & D_{i,yz}^k \\ D_{i,zx}^k & D_{i,zy}^k & D_{i,zz}^k \end{bmatrix}, \qquad (10)$$

where the diagonal and off-diagonal tensor elements are of the form

$$D_{i,xx}^k = \frac{D_{0i}^{\ k}}{\tau^k} + \frac{\left(\alpha_\ell^k - \alpha_t^k\right)}{\phi \, S^k \left|\vec{u}^k\right|} \left(u_x^k\right)^2 + \alpha_t^k \, \frac{\left|\vec{u}^k\right|}{\phi \, S^k} \qquad (11)$$

$$D_{i,xy}^k = \frac{\left(\alpha_\ell^k - \alpha_t^k\right)}{\phi \, S^k \left|\vec{u}^k\right|} \, u_x^k \, u_y^k \qquad (12)$$

$$\left|\vec{u}^k\right| = \left[\left(u_x^k\right)^2 + \left(u_y^k\right)^2 + \left(u_z^k\right)^2\right]^{1/2} \,. \qquad (13)$$

Note that the tortuosity of phase k, τ^k, is related to the formation resistivity factor F through the equation

$$\tau^k = F \, \phi \, S^k \,. \qquad (14)$$

Three phase flash calculation. Dissolution of gaseous components into an aqueous phase and water vaporization into a gas phase may alter composition of withdrawn gas. The simulator implements three-phase flash calculation by Eqs. (4) through (7) to reproduce these phenomena.

The fugacity coefficients of each component in gas and oil phases, φ_i^g and φ_i^o shown in Eq. (4), are calculated using EOS as are calculated in conventional compositional simulators. The fugacity of each component in an aqueous phase needs to be approximated to calculate a component molar fraction in an aqueous phase (w_i) from that in a gas phase (y_i). The fugacity of the water component in an aqueous phase is given by Lewis-Randall rule [6], while that of a gaseous solute is given by Henry's law as

$$f_i^w = w_i k_i \,; \quad i \neq w \,. \qquad (15)$$

The thermodynamic definition for Henry's law constant together with the fundamental differential equation definition of fugacity leads to the following differential equation relating the variation of Henry's law constant with temperature and pressure [6]:

$$k_i = \lim_{w_i \to 0} \frac{f_i^w}{w_i} \,. \qquad (16)$$

$$d(\ln k_i) = \frac{v_i^{w\infty}}{RT} dp + \frac{H_i^g - H_i^{w\infty}}{RT^2} dT \,. \qquad (17)$$

The term $H_i^g - H_i^{w\infty}$ depends strongly on temperature and no general correlation describing its change with respect to temperature is available. On the other hand, $v_i^{w\infty}$ is usually not significantly sensitive to pressure. Hence Eq. (17) is considered at a constant temperature and integrated with respect to pressure from the limits p^0 to p, which gives

$$\ln k_i = \ln k_i^0 + v_i^{w\infty} (p - p_i^0) / (RT) \,. \qquad (18)$$

The simulator uses Eq. (18) to calculate Henry's law constant at the specified temperature and pressure, given an input reference Henry's law constant, k_i^o, at the same temperature and another pressure.

Using the improved PVT simulator, the reference Henry's law constants for gaseous components in salt water are approximated applying the scaled particle theory (SPT) as described in Appendix A. Furthermore, the reference Henry's law constants thus estimated can be tuned through regression with measured gas solubility data.

Adsorption. A reservoir rock provides surface areas for gas adsorption, which may result in the change in withdrawn gas composition. This surface area for adsorption is significant for tight gas reservoirs where the small pore size offers large internal surface areas or for reservoirs with a large quantity of clay minerals.

The simulator reproduces a mono-layer multi-component adsorption/desorption system using the extended Langmuir isotherm [7].

$$\omega_i = \frac{\omega_{i,max} \, B_i \, y_i \, p}{1 + p \sum_j B_j \, y_j} \,, \qquad (19)$$

which is used in Eq. (8). In the UGS simulator, the constants $\omega_{i,max}$ and B_i can be specified independently for sand and shale together with shale content at each grid block.

Non-Darcy flow. Since withdrawal and injection gas rates are expected much larger in a UGS operation than those in an ordinary gas field operation, turbulent flow may be of importance and is reproduced in the simulator. High velocity gas flow in porous media can be modeled with the Forchheimer equation given by

$$-\nabla\Phi^{g} = \frac{\mu^{g}}{k\,k_{r}^{g}}\vec{u}^{g} + \beta\,\tilde{\rho}^{g}\left|\vec{u}^{g}\right|\vec{u}^{g}, \tag{20}$$

which is written as a form of Darcy's law as

$$-\nabla\Phi^{g} = \frac{\mu^{g}}{k\,k_{r}^{g}}\left(1+F_{o}\right)\vec{u}^{g} \tag{21}$$

$$F_{o} = \beta\,k\,k_{r}^{g}\,\tilde{\rho}^{g}\left|\vec{u}^{g}\right| / \mu^{g}, \tag{22}$$

where β is referred to as the non-Darcy flow coefficient or the turbulence factor. The simulator approximates β based on the correlations by Geerstma [8] and Frederick and Graves [9].

In addition to turbulent flow, Darcy's law requires a correction at a low pressure gas flow, which is known as the Klinkenberg effect. This effect is expressed by altering the absolute permeability as

$$k = k_{\infty}\left[1+\left(b/p\right)\right] \tag{23}$$

The simulator reproduces non-Darcy flow including both the turbulent flow and Klinkenberg effect with the combination of Eqs. (21) and (23).

$$k = k_{\infty}\left[\frac{1+\left(b/p\right)}{1+F_{o}}\right] \tag{24}$$

Tensorial permeability. A corner point grid system with local grid refinement (LGR) is available in the UGS simulator. When highly distorted grid blocks are applied, erroneous performance may be calculated by the usual corner point grid formulation because of the inaccurate evaluation of fluid flux between grid blocks.

The UGS simulator adopts a more general transmissibility formulation using MPFA than that used in conventional simulators. MPFA was designed to calculate reasonable transmissibilities in the presence of skewed grid blocks in a corner point grid system and also allows incorporation of permeability tensors even when their principal directions are not aligned with the grid [10]. The introduction to MPFA is given in Appendix B.

Fig. 2 shows the oil saturation distribution simulated for WAG injection in an anisotropic (permeability in y-direction is ten times greater than that in x-direction) but homogeneous hypothetical reservoir. Although the calculated oil saturation distribution must be symmetric, it skewed when highly distorted corner point grid blocks are applied with the conventional transmissibility formulation. On the other hand, MPFA remarkably improved the calculation results.

TVD scheme. It is well known that the single-point upstream approximation introduces numerical dispersion. To rigorously evaluate the mixing between gases, overestimate of it should be avoided by suppressing numerical dispersion. The simulator has an option to discretize flux terms using the TVD scheme to reduce numerical dispersion [11] (Appendix C). The TVD scheme can be applied to Cartesian/cylindrical coordinates, irregular grid system, corner point grid system and LGR.

Fig. 3 shows how effective the TVD scheme is to reduce numerical dispersion in the case of oil-water displacement with unit mobility ratio in a 2-D model with LGR.

Temperature calculation. Reduction in reservoir temperature is expected by injecting vaporized LNG of low temperature and by adiabatic expansion associated with huge volume of gas withdrawal. The simulator has a function to calculate reservoir temperature taking account of these effects as shown in Eq. (2).

In addition, it is desirable to approximate wellbore temperature to diagnose the necessity of installing a wellhead heater to avoid gas hydration. The simulator calculates wellbore pressure and temperature by solving the following Bernoulli type equation based on the assumption that the flow is steady state in a straight string with a constant diameter.

$$\frac{d}{dz}\left(H+\frac{1}{2}v^{2}+gz\cos\theta\right) = -F_{t} - (h/\tilde{\rho}Av)(T-T_{0}) \tag{25}$$

The above equation can be split into the mechanical energy balance equation and thermal energy balance equation as

$$V\frac{dp}{dz}+v\frac{dv}{dz}+g\cos\theta = -F \tag{26}$$

$$T\frac{dS}{dz} = F_{i} - (h/\tilde{\rho}Av)(T-T_{0}), \tag{27}$$

which is reduced, by applying the chain rule, to the following system of ordinary differential equations:

$$\begin{bmatrix} 1+\tilde{\rho}v\dfrac{\partial v}{\partial p} & \tilde{\rho}v\dfrac{\partial v}{\partial T} \\ \dfrac{\partial S}{\partial p} & \dfrac{\partial S}{\partial T} \end{bmatrix} \begin{bmatrix} \dfrac{dp}{dz} \\ \dfrac{dT}{dz} \end{bmatrix} = \begin{bmatrix} -\tilde{\rho}\left(F+g\cos\theta\right) \\ \left[F_{i}-\left(h/\tilde{\rho}Av\right)\left(T-T_{0}\right)\right]/T \end{bmatrix}. \tag{28}$$

The simulator solves Eq. (28) to obtain pressure and temperature profiles with fluid and thermodynamic properties calculated by EOS.

Example Applications

The UGS simulator thus developed was first validated through the test runs with laboratory experiment data. The simulator was then applied to predict UGS performances in a hypothetical reservoir followed by the calculation using an actual reservoir structure.

Some of these runs are described below.

Validation with Experiment Data

Japan Petroleum Exploration Co., Ltd. (JAPEX) conducted laboratory experiments including the measurements of dispersion in slimtube displacement and gas solubility into water. These experiments were simulated to validate how the simulator can reproduce experimental results.

Slimtube test for dispersion. One of the slimtube tests, in which argon displaces methane filled in a 40 ft long slimtube with 1/4 inch OD, was simulated using a 1-D model composed of 100 grid blocks. As depicted in Fig. 4, it is impossible to reproduce effluent concentration of each component using the conventional (single point upstream) approximation because of numerical dispersion. This experiment can be reproduced, without further refining grid blocks, by the combination of TVD scheme and the function for calculating physical dispersion.

In the case of the grid system applied to this simulation, the numerical dispersion (dispersivity) with TVD scheme was 0.007 ft, which is equivalent to the Peclet number of 6000. It was found that calculation with the TVD scheme could accurately represent actual physical dispersion for the Peclet number smaller than this value down to 50. For example, effluent argon concentration simulated with physical dispersivity of 0.04 ft (Peclet number 1000) satisfactorily agreed with the measured data.

Gas Dissolution into salt water. The solubility of synthesized gas composed of N_2 (0.02%), C_1 (95.91%), C_2 (3.11%) and C_3 (0.96%) into 30000 mg/L salt water at 50°C was simulated. Fig. 5 presents the calculated methane and ethane solubilities along with the measured data.

The solubility predicted based on the fugacity estimated with the Henry's law constant for pure water, which is calculated in most of conventional compositional simulators, deviated from the measured data. On the other hand, the solubility predicted with the Henry's law constant approximated by the SPT resulted in good agreement with the measured data. This indicates that the simulator can accurately estimate the solubility of gaseous components into salt water even without measured data. When measured data are available, the Henry's law constant is to be further tuned through regression as other EOS parameters are.

Hypothetical Reservoir Cases

A hypothetical reservoir model that had a shape of a simple dome was constructed to validate the applicability of the simulator to problems of a practical size as well as to provide a guide for the effects of noteworthy physical phenomena on withdrawn gas composition. The 3-D and cross sectional views of this model are illustrated in Fig. 6 and the specifications of the model is given in Table 1.

As also summarized in Table 1, most case studies were conducted based on the following scenarios:

- The reservoir is depleted at the gas recovery of 80%.
- A certain volume of nitrogen is then injected as cushion gas from injection wells located on the down flanks.
- Methane is injected from the wells located at the crest till the sum of in place volumes of methane and nitrogen becomes identical to the original gas in place (OGIP)
- Certain volume of cyclic operation (withdrawal, shut-in, injection, shut-in every three months) is repeated.

In situ gas composition. The effect of in situ gas composition was investigated assuming the following three types of initial gas composition:

Gas A: C_1 (90%), C_3 (10%)
Gas B: C_1 (95%), C_3 (2%), C_7 (2%), C_{10} (1%)
Gas C: C_1 (85%), C_3 (5.5%), C_7 (5.5%), C_{10} (4%).

In these cases for studying the effect of initial gas composition, methane was directly injected into the depleted reservoir (80% of recovery) without inert cushion gas followed by the cyclic UGS operation with working volumes (volume of gas withdrawn or injected during three months) of 15, 20 and 30% of OGIP. At the end of the first withdrawal with the working volume of 30%, condensate is expected to accumulate at about 2 and 5% of reservoir fluid saturation for Gases B and C, respectively, while Gas A is dry throughout the operation.

Fig. 7 plots the predicted heating values of withdrawn gases. Although the heating values vary with time, this figure shows those averaged in each withdrawal period. The results are summarized as:

- Heating value of withdrawn gas increases at first as heavier components, which has been driven away from the wells during injection, diffuse back toward the wells. It decreases with increase in methane content in the reservoir after several cyclic operations.
- When condensate accumulates in the vicinity of wells during initial production, heating value of withdrawn gas increases faster because of the production of condensate vaporized by methane injection.
- The average heating value during a withdrawal period increases by 1-2% for Gases B and C. No remarkable change was observed in the case of Gas A. The maximum heating value during a withdrawal period is slightly higher than the average value by about 0.5%.
- The working gas volume does not significantly affect the change in withdrawn gas composition so far as it is less than 30% of OGIP.

Gas dissolution. For the reservoir filled with Gas C, the heating values of withdrawn gases were simulated assuming the methane solubility into water of 0.11 mole% at 10 MPa (measured data) as well as those increased by the factors of 10 and 100. The operation scenario is identical to that with the working volume of 20% OGIP described above.

As shown in Fig. 8, no remarkable difference in heating value profiles was observed even if solubility ten times larger was applied. Solubility of gaseous components affected bottomhole pressure performance rather than heating value.

Cushion gas volume. In the series of cases for this factor, nitrogen cushion gas was injected from the wells located on the down flanks followed by methane injection, after 80% of initial gas (pure methane) was recovered. Cushion gas volumes were assumed to be 10, 20 and 30% of OGIP. Nitrogen content in withdrawn gas was predicted with working volumes of 15, 20 and 30% of OGIP for each cushion gas volume.

The average effluent nitrogen content during each withdrawal period (Fig. 9) suggests the following:

- The nitrogen content primarily depends on cushion gas volume.
- Cushion gas may breakthrough at early stage even if cushion gas volume is as small as 10% of OGIP.
- The average nitrogen content becomes only 2% even with cushion gas of 30% OGIP. However, instantaneous nitrogen content reaches 7% at its maximum.
- When both the cushion gas and working gas volumes are 30% of OGIP, 20% of nitrogen is produced in the first ten years.

Dispersivity. The effect of longitudinal dispersivity was investigated for the case of nitrogen cushion gas of 20% of OGIP and working gas volume of 20% of OGIP. The other conditions including operation scenario were the same as above.

Fig. 10 shows the predicted average nitrogen content in withdrawn gas corresponding to the dispersivity of 0.5, 1, 5, 10 and 20 ft. Breakthrough of nitrogen was hastened and nitrogen content built up more rapidly with the increase in dispersivity.

Reservoir heterogeneity. The reservoir performances were simulated assuming five types of absolute permeability distributions. All of these permeability distribution models have the average value of 500 md and heterogeneity with Dykstra-Persons coefficient of 0.6. These models, however, were constructed applying a geostatistical approach (sequential Gaussian simulation) based on the variograms indicating different ranges as listed below. Hence these models have different continuity both in horizontal and vertical directions. In all the models, vertical permeability was assumed to be one tenth of horizontal permeability. The other conditions are the same as above.

Model	Range (ft)	
	Horizontal	Vertical
A	200	20
B	1000	20
C	2000	20
D	200	40
E	200	100

Fig. 11 shows the predicted effluent nitrogen content. Since cushion gas advances toward the wells from the bottom of the reservoir in a manner similar to coning phenomena, more significant breakthrough occurred with the increase in vertical/horizontal range ratio.

Actual Reservoir Case

The UGS simulator was next applied to the simulation assuming that UGS is conducted in one of the actual Japanese gas reservoirs owned by Japan Energy Development Co., Ltd, (JE). The brief description of this reservoir is given in Table 2. The reservoir and fluid models were established by JE using $50 \times 65 \times 2$ grid blocks with LGR in the vicinity of well locations (Fig. 12 and Table 2).

Simulation was conducted based on hypothetical well locations and operation scenario. As shown in Table 2, three wells are assumed to be drilled on the down flanks to inject nitrogen cushion gas. Three month cyclic UGS operation is then assumed to be implemented at nine wells located at the crest of the reservoir with working volume of 20% of OGIP, after filling the reservoir with 20 % remaining in situ gas, 20% nitrogen and 60% of methane.

Fig. 13 shows the simulated heating value at the injection/withdrawal wells. The wells near cushion gas encounter significant reduction in heating value of withdrawn gas due to mixing with nitrogen. The average heating value decreases by more than 2% after 10 year operation, which is more significant than that expected in the hypothetical reservoir cases. It is obvious to re-consider the operation scenario to minimize the amount of associated nitrogen production by investigating the sensitivity to the parameters such as cushion gas volume and withdrawal rate. This study shows promise that the UGS simulator is useful and applicable for such studies.

Conclusions

The UGS simulator was developed, which can rigorously evaluate a heating value of withdrawn gas taking into consideration all the major phenomena that possibly affect composition of withdrawn gas. The functions newly developed for the UGS simulator were then validated through test runs with laboratory tests and through field scale simulations for hypothetical and actual reservoirs.

1. The test run results revealed that the new functions could successfully reproduce the expected physical phenomena and reduce numerical errors.

2. Field scale simulations with a hypothetical reservoir model indicated that remaining in situ gas composition, cushion gas volume and reservoir heterogeneity significantly affected composition of withdrawn gas. Working gas volume was less influential so far as it was less than 30% of OGIP. Gas dissolution into water affected bottomhole pressure performance rather than withdrawn gas composition.

3. The simulation with an actual reservoir structure

suggested the necessity of investigation of well-by-well performance to optimize UGS operation.

4. The laboratory and field scale simulations give promise that the UGS simulator is useful and applicable to sophisticated evaluation of a UGS operation including prediction of withdrawn gas composition.

Nomenclature

A = tubing cross sectional area, L^2
b = constant for Klinkenberg effect, Lt^2/M
B = Langmuir isotherm parameter, Lt^2/M
c_R = heat capacity of rock matrix per unit volume, M/Lt^2T
d = depth, L
D = total dispersion coefficient, L^2/t
D_0 = molecular diffusion coefficient, L^2/t
f = fugacity, M/Lt^2
F = formation resistivity factor
F = mechanical energy converted to thermal energy per unit fluid mass and tubing length ($F_i + F_t$), L^3/t^2
F_i = mechanical energy converted to fluid thermal energy per unit fluid mass and tubing length, L^3/t^2
F_o = Forchheimer number
F_t = mechanical energy lost to tubing per unit fluid mass and tubing length, L^3/t^2
g = gravity acceleration, L/t^2
h = heat transfer coefficient, ML/t^3T
H = phase molar enthalpy, ML^2/t^2mol
H = enthalpy per unit mass, L^2/t^2
H_i = molar enthalpy of component i, ML^2/t^2mol
J = dispersive flux, mol/L^2t
k = absolute permeability, L^2
k = Henry's law constant, M/Lt^2
K = equilibrium ratio
k_r = relative permeability
k_∞ = liquid absolute permeability, L^2
N = number of moles per unit reservoir volume, mol/L^3
N_a = number of adsorbed moles per unit reservoir volume, mol/L^3
p = pressure, M/Lt^2
P_c = capillary pressure, M/Lt^2
$\tilde{q}$ = well molar flow rate per unit reservoir volume, mol/L^3t
$\tilde{Q}_{loss}$ = heat loss rate to surroundings per unit reservoir volume, M/Lt^3
R = ideal gas constant, ML^2/t^2Tmol
S = phase saturation
S = entropy per unit mass, L^2/t^2T
t = time, t
T = temperatute, T
u = superficial velocity, L/t
U = phase molar internal energy, ML^2/t^2mol
v = fluid velocity in tubing, L/t
V = fluid volume per unit mass, L^3/M
v_i = partial molar volume of component i, L^3/mol
w = mole fraction in aqueous phase
x = mole fraction in oil phase
y = mole fraction in gas phase
z = location in tubing, L
α = dispersivity, L
β = non-Darcy flow coefficient, 1/L
γ = phase specific weight, M/L^2t^2
θ = tubing angle from the vertical
κ = total conductivity of rock and fluid, ML/t^3T
μ = phase viscosity, M/Lt
ρ = phase molar density, mol/L^3
$\tilde{\rho}$ = mass density, M/L^3
τ = tortuosity
ϕ = porosity
φ = fugacity coefficient
Φ = potential, M/Lt^2
ω = number of adsorbed moles per unit rock mass, mol/M

Superscript
k = phase number
g, o, w = gas, oil, water phases
0 = reference
$w\infty$ = aqueous phase at infinite dilution

Subscript
i = component number
ℓ = longitudinal
max = maximum
R = rock matrix
t = transverse
x, y, z = x, y, z directions
0 = reference

Acknowledgement

The authors gratefully acknowledge JNOC and Information Center for Petroleum Exploration and Production (ICEP) for financial support and permission to present this paper. They wish to thank Japan oil Engineering Co, Ltd. (JOE) and CMG for their technical support.

They also acknowledge JE for providing them with the field data as well as the reservoir model, JAPEX for presenting laboratory experiment data and Teikoku Oil Co., Ltd. for helpful technical discussions.

References

1. Cornot-Grandolphe, C.: "Underground Gas Storage in the World," Proceedings of IEA Conference on Natural Gas Technologies: Energy Security, Environment and Economic Development, Kyoto, Japan (Oct. 31-Nov. 3, 1993).
2. Nacul, E.C., Gilmore Jr., R.G., and Theodos, A.F.: "Simulation of Crawford Gas Storage Field," paper SPE29157 presented at 1994 Eastern Regional Conference and Exhibition, Charleston, WV, Nov. 8-10.

3. Sonier, F, Nabil, R.: “Case Study of Gas BTU Control For Operational Strategy and Inert Gas Injection Planning,” paper SPE49220 presented at 1998 SPE Annual Technical Conference and Exhibition, New Orleans, LA, Sep. 27-30.
4. Sonier, F, Nabil, R.: “Full-Field Gas Storage Simulation Using a Control-Volume Finite-Element Model,” paper SPE26655 presented at 1993 SPE Annual Technical Conference and Exhibition, Houston, TX, Oct. 3-6.
5. Lake, L.W.: Enhanced Oil Recovery, Prentice-Hall Inc., Englewood Cliffs, NJ (1989).
6. Smith, J.M., and Van Ness, H.C.: Introduction to Chemical Engineering Thermodynamics, Fourth Edition, McGraw-Hill, New York, NY (1987).
7. Hall, F.E., Zhou, C., Gasem, K.A.M., Robinson Jr., R.L., and Yee, D.: “Adsorption of Pure Methane, Nitrogen, and Carbon Dioxide and Their Binary Mixtures on Wet Fruitland Coal,” Paper SPE 29194 presented at 1994 Eastern Regional Conference & Exhibition, Charleston, WV, Nov. 8-10.
8. Geertsma, J.: “Estimating the Coefficient of Inertial Resistance in Fluid Flow Through Porous Media,” SPEJ (Oct. 1974) 445-450.
9. Frederick Jr., D.C., and Graves, R.M.: “New Correlations To Predict Non-Darcy Flow Coefficients at Immobile and Mobile water Saturation,” Paper SPE 28451 presented at 1994 Annual Technical Conference and Exhibition, New Orleans, LA, Sep. 25-28.
10. Aavatsmark, I., Barkve, T., and Mannseth, T.: “Control-Volume Discretization Methods for 3D Quadrilateral Grids in Inhomogeneous Anisotropic Reservoirs,” Paper SPE38000 presented at 1997 SPE Reservoir Simulation Symposium, Dallas, TX, June 8-11.
11. Edwards, M.G., and Rubin, B.: “Total Variation Diminishing Schemes and the Two-Point Upstream Mobility Weighting Scheme,” Unsolicited Paper SPE 23947 (1991).
12. Pierotti, R.A.: “A Scaled Particle Theory of Aqueous and Nonaqueous Solutions,” *Chemical Reviews* (1976) **76**, 717-726.
13. Li, Y.-K. and Nghiem, L.X.: “Phase Equilibria of Oil, Gas and Water/Brine Mixtures from a Cubic Equation of State and Henry's Law,” *Can. J. Chem. Eng.* (June 1986) **64**, 486-496.

Appendix A Calculation of Henry’s Law Constant by Scaled Particle Theory

This appendix describes the method to predict Henry’s constants for gases in brines using SPT [12] when experimental data are not available [13].

The SPT can be used to obtain the following expression for Henry’s law constant:

$$\ln\left(\frac{k_i v_s}{RT}\right)=\left(\frac{G_{bi}}{RT}\right)+\left(\frac{G_{ai}}{RT}\right), \tag{A1}$$

where

G_{bi} = partial molar Gibbs energy of cavity formation
G_{ai} = partial molar Gibbs energy of interaction
v_s = molar volume of pure solvent.

The energy of cavity formation is the work required to create a cavity in the solvent of suitable size to accommodate the solute molecule, and the energy of interaction is the molar Gibbs energy resulting from the interaction of the solute molecule with the surrounding solvent molecules.

The expression for the energy of cavity formation for gas solubility in brine is given by

$$\begin{aligned}\frac{G_{bi}}{RT} &= -\ln(1-\theta_3)+\frac{3\theta_2}{1-\theta_3}\sigma_i^* \\ &+\left[\frac{3\theta_1}{1-\theta_3}+\frac{9}{2}\frac{\theta_2^2}{(1-\theta_3)^2}\right](\sigma_i^*)^2+\frac{p}{RT}\frac{\pi}{6}\eta_w(\sigma_i^*)^3\end{aligned} \tag{A2}$$

where

$$\theta_n \equiv \frac{\pi}{6}\eta_w\sum_j \rho_j(\sigma_j^*)^n\ ; \quad n=1,2,3 \tag{A3}$$

$$\sigma_k^* \equiv \sigma_k/\sigma_w\ ; \quad k=i,\ j \tag{A4}$$

$$\eta_w = N\sigma_w^3 \tag{A5}$$

σ_I = molecular diameter of species i in the solvent
σ_w = molecular diameter of pure water
N = Avogadro’s number
ρ_j = molar density of species j in the solvent

The summation in equation (A3) is over all species present in the solvent. For the case of brine with dissolved gases, this includes the gaseous solutes, pure water, and the ionic components of any salts present.

The energy of interaction is expressed as

$$\begin{aligned}\frac{G_{ai}}{RT} &= -\frac{32}{9}\frac{\pi}{T}\eta_w\sum_j\frac{\varepsilon_{ij}}{k}\rho_j(\sigma_{ij}^*)^3 \\ &-\frac{4}{3}\frac{\pi}{kT}\frac{\rho_w N\mu_w^2(N\alpha_i)}{(\sigma_{iw}^*)^3\eta_w}\end{aligned} \tag{A6}$$

where

$$\varepsilon_{ij}=\sqrt{\varepsilon_i\varepsilon_j} \tag{A7}$$

$$\sigma_{ij}^* = F(\sigma_i^*+\sigma_j^*)/2 \tag{A8}$$

μ_w = dipole moment of water
α_I = polarizability of solute i
k = Boltzmann’s constant
ε_I = Lennard-Jones energy parameter for component i

The function F is given by

$$F(T)=16280/T^2-141.75/T+1.2978 \tag{A9}$$

Eqs. (A2) and (A6) require the molar volume of water and the ions. For aqueous NaCl solutions these are estimated as follows

$$\rho_w = (1 - w_{NaCl})\tilde{\rho}_s / M_w \qquad \text{(A10)}$$

$$\rho_{Na^+} = \rho_{Cl^-} = w_{NaCl}\tilde{\rho}_s / M_{NaCl} \qquad \text{(A11)}$$

where

M_w = molecular weight of water
M_{NaCl} = molecular weight of NaCl
$\tilde{\rho}_s$ = mass density of aqueous NaCl solution
w_{NaCl} = mass fraction of NaCl in water

Appendix B Fluid Flux Calculation by MPFA

This appendix describes an implementation MPFA method based on the work by Aavatsmark, et al. [10].

A Corner Point grid is made up of quadrilaterals defined by an assignment of 8 corners per cell, where each corner point is associated with a given triple of values that gives its location with respect to a fixed coordinate system. When inter-cell transmissibilities are to be computed, a group of cells must be considered. Rather than considering just pairs of cells, a cell template like that shown in the figure below is required.

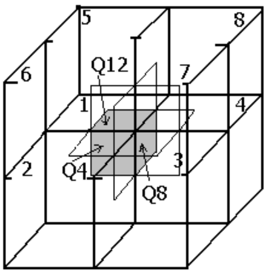

Cell 1 in the above is a typical corner point cell (but drawn in a regular manner for clarity) and Cells 2, 4 and 5 are cells to which Cell 1 is going to be connected to allow fluid flow. Transmissibilities are built up by quarter faces from which the complete transmissibilities can be assembled. The final transmissibilities will depend on the properties of the 8 cells shown.

First, nodes are placed at the barycenter of the cell. Barycenters are identified for the faces as well. The method then uses a piece-wise trilinear description for the overall phase potential (oil phase pressures plus heads plus capillary pressures) in each quadrant, based on known potential values at the cell nodes:

$$p = A_0 + A_1 x + A_2 y + A_3 z\,, \qquad \text{(B1)}$$

where p denotes one of the phase potentials (oil, water, or gas) and the $\{A_i\}$ are coefficients that depend on the potential's nodal values, as well as cell geometries and permeabilities. To define ∇p, it suffices to define the three values for the inner products of ∇p with respect to three linearly independent vectors, such as the center-to-face vectors.

Eight ∇p vectors will be defined, one for each subregion, in an inter-related manner in terms of the eight nodal values and various cell-related geometric information. Thus, there will be $3\times8=24$ values to be determined, and hence 24 conditions are required. This will give a piece-wise representation for the potential P over the entire interaction region.

There are 12 subfaces lying between the subregions, and each subface represents a quarter of some full face that lies between the cells of the template. These subfaces have the full face's barycenter as one of their corners. The following continuity conditions will be imposed at these centers:

(I) Potential P is continuous at the barycenter for each of the 12 faces;
(II) Flow normal to the face is continuous at the barycenter for each of the 12 faces.

Thus, two continuity conditions have been specified at the 12 face barycenters, for a total of 24 conditions. Note that the flow continuity conditions will involve permeabilities, through a permeability tensor, and an application of Darcy's law. In fact, it can be seen that Condition (I) can always be written as a linear expression involving the constants ∇ P that are being set equal to some difference in nodal values. As for condition (II), Darcy's law is used to equate the normal component of the fluid velocities:

$$\vec{u} \bullet \left[\vec{\vec{k}}^{(1)} \nabla p^{(1)} \right] = \vec{u} \bullet \left[\vec{\vec{k}}^{(2)} \nabla p^{(2)} \right], \qquad \text{(B2)}$$

where $\vec{\vec{k}}^{(i)}$ is the permeability tensor assigned to Cell i and $\vec{u}$ is the unit vector normal to the face. The results are linear expressions involving the components of $\nabla p^{(i)}$. These equations can be set up and solved. After this solution is complete, the Darcy velocity normal to the face is calculated as $\vec{u} \bullet \left(\vec{\vec{k}} \nabla p \right)$ at the barycenter of the face, where ∇p is computed from the piecewise representation of p. It does not matter from which side of the face the velocity is calculated, as the continuity condition on velocity ensures that the values will be the same. To obtain a volumetric flow rate for this quarter face, the overlap area is used to multiply the velocity.

Note that 8 values of the potential are involved, but that fluid flow only occurs between the base cell and its 6 neighbors, which means that this method has a flow stencil that is the same as the 7-point (3 dimensions) or the 5-point (2 dimensions) techniques usually used in simulators. Thus, the Darcy velocities in this approach are immediately associated with fluid flows across faces between contacting cells that have well defined overlap areas. Thus, an upstream flow properties evaluation method can easily be applied to the flows for the multi-phase situation.

Thus, this method is capable of representing Darcy velocities as a full tensor applied to a proper potential gradient vector and permits accurate normal face flows to be computed. This method becomes (up to) a 9-point method in 2 dimensions and a 27-point method in 3 dimensions.

Appendix C Fluid Flux Calculation by TVD Scheme

This appendix describes the TVD scheme and its expansion to an irregular grid system.

When $-\dfrac{\partial p}{\partial x} > 0$, the flux of component j in an oil phase between grid blocks I and I+1 is calculated with the TVD schemes by the following form:

$$F^n_{jo,\,I+1/2} = f^n_{jo,\,I} + \tfrac{1}{2}\,\theta\left(r^n_{jo,\,I}\right)\Delta f^n_{jo,\,I+1/2}, \tag{C1}$$

where $f^n_{jo,\,I}$ is the single-point upstream flux given by

$$f^n_{jo,\,I} = T^n_{jo,\,I}\left(p_I - p_{I+1}\right) \tag{C2}$$

and

$$\Delta f^n_{jo,\,I+1/2} = f^n_{jo,\,I+1} - f^n_{jo,\,I}\,. \tag{C3}$$

The function $\theta(r)$ is called a flux limiter and is a function of the neighboring flux gradients $r^n_{jo,\,I}$ defined as

$$r^n_{jo,I} = \frac{\Delta f^n_{jo,\,I-1/2}}{\Delta f^n_{jo,\,I+1/2}}\,. \tag{C4}$$

The flux limiter known as a Fromm’s limiter is given by [11]

$$\theta(r) = \max\left(\min\left(2r,\, \tfrac{1}{2}(r+1),\, 2\right),\, 0\right), \tag{C5}$$

which provides a third order accuracy in space whenever

$$\theta(r) = \tfrac{1}{2}(r+1)\,. \tag{C6}$$

To expand the above mentioned TVD scheme to an irregular grid system, Eqs. (C1), (C4) and (C5) are replaced with the following Eqs. (C7), (C8) and (C9), respectively.

$$F^n_{jo,\,I+1/2} = f^n_{jo,\,I} + \frac{1}{2}\lambda_{I+1/2}\,\theta\left(r^n_{jo,\,I}\right)\Delta f^n_{jo,\,I+1/2} \tag{C7}$$

$$r^n_{jo,I} = \frac{\Delta f^n_{jo,\,I-1/2} \big/ \left(\Delta x_{I-1} + \Delta x_I\right)}{\Delta f^n_{jo,\,I+1/2} \big/ \left(\Delta x_I + \Delta x_{I+1}\right)} \tag{C8}$$

$$\theta(r) = \max\left(\min\left(\frac{2}{\lambda_{I-1/2}}r,\, \frac{(r+1)}{2},\, \frac{2}{\lambda_{I+1/2}}\right),\, 0\right), \tag{C9}$$

where

$$\lambda_{I-1/2} = \frac{\Delta x_I}{(\Delta x_I + \Delta x_{I-1})/2} \tag{C10}$$

$$\lambda_{I+1/2} = \frac{\Delta x_I}{(\Delta x_I + \Delta x_{I+1})/2}\,. \tag{C11}$$

SI Metric Conversion Factors

ft × 3.048* E-01 = m
md × 9.869 233 E-04 = µm
inch × 2.54* E+00 = cm

* Conversion factor is exact.

Table 1 Specifications of hypothetical reservoir model study

Reservoir Description	
Area	2×10^6 m^2
Thickness	50 m
Porosity	0.2
Horizontal Permeability	500 md (constant)
Vertical Permeability	50 md (constant)
Initial Pressure	10 MPa
Depleted Pressure	2 MPa (Gas recovery: 80%)
Original Gas in Place	2×10^9 std m3
Temperature	320 K
Production/Injection Scenario	
Number of Wells	4 UGS wells, 4 N_2 injectors
Production/Injection Schedule	1. production of 80% in situ gas 2. injection of 20% N_2 3. injection of 20% CH_4 4. Cyclic UGS operation (withdrawal, shut-in, injection, shut-in for every three months)
Model Description	
Number of Grid Blocks	31 x 31 x 30
Physical Dispersion	No

Table 2 Specifications of acutual reservoir model study

Reservoir Description	
Thickness	0 - 200 m
Av. Porosity	0.14
Av. Horizontal Permeability	85 md
Av. Vertical Permeability	8.5 md
Initial Pressure	10 MPa
Depleted Pressure	2 MPa (Gas recovery: 80%)
Initial Fluid Composition	C_1:98.5%, C_2:0.18%, C_3:0.03%, C_4:0.01%, C_{5+}:0.01%, CO_2:1.22%, N_2:0.5% (dry gas)
Temperature	330 K
Production/Injection Scenario	
Number of Wells	9 UGS wells, 3 N_2 injectors
Withdrawal/Injection Schedule	1. production of 80% in situ gas 2. injection of 20% N_2 3. injection of 20% CH_4 4. Cyclic UGS operation (withdrawal, shut-in, injection, shut-in for every three months)
Model description	
Number of Grid Blocks	50 x 65 x 2 + 6675 of LGR blocks
Physical Dispersion	No

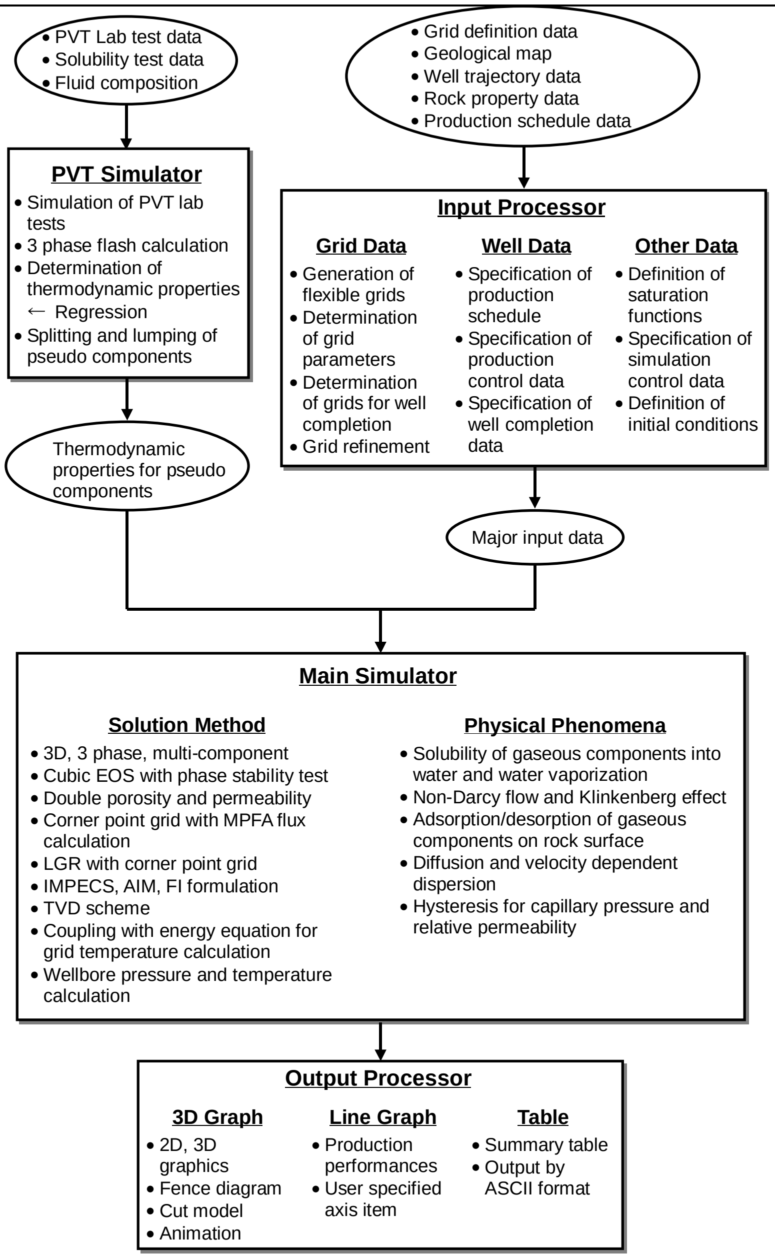

Fig.1 Configuration of UGS simulator

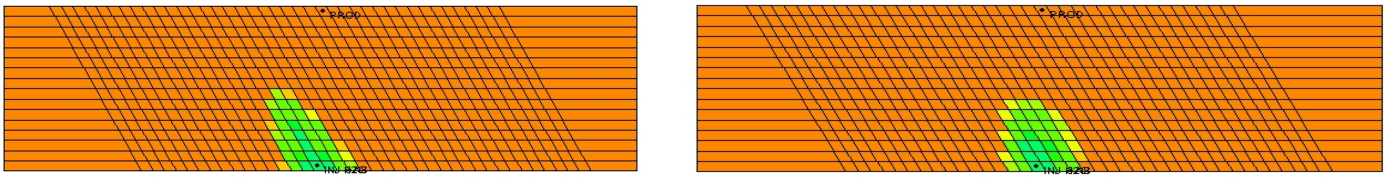

without MPFA **with MPFA**

Fig.2 Water saturation distribution (with and without MPFA)

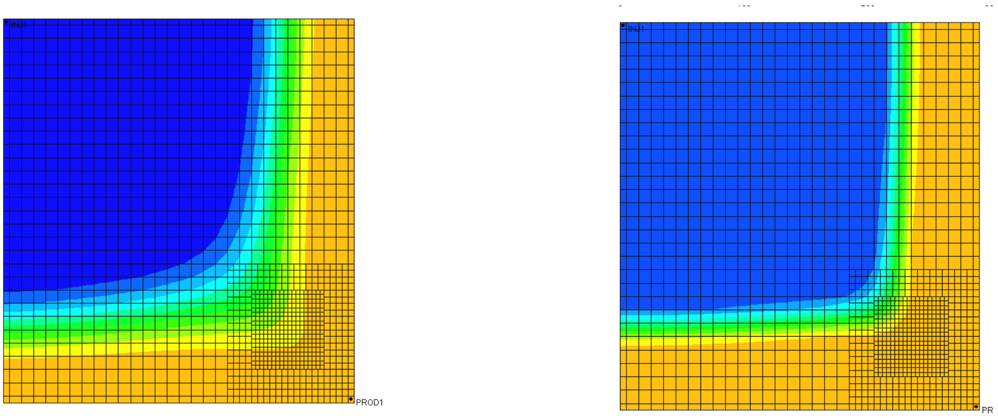

without TVD **with TVD**

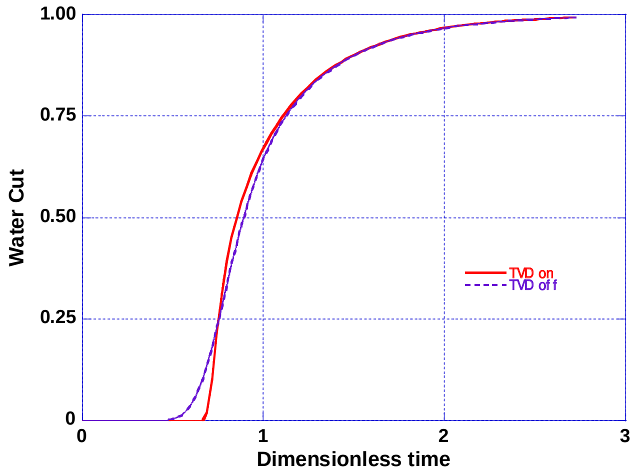

Water cut

Fig.3 Effect of TVD method in LGR model

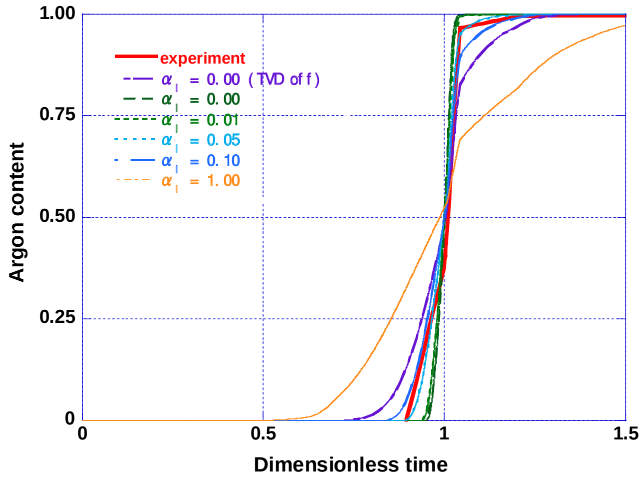

Fig4. Simulated slimtube test results along with experiment data

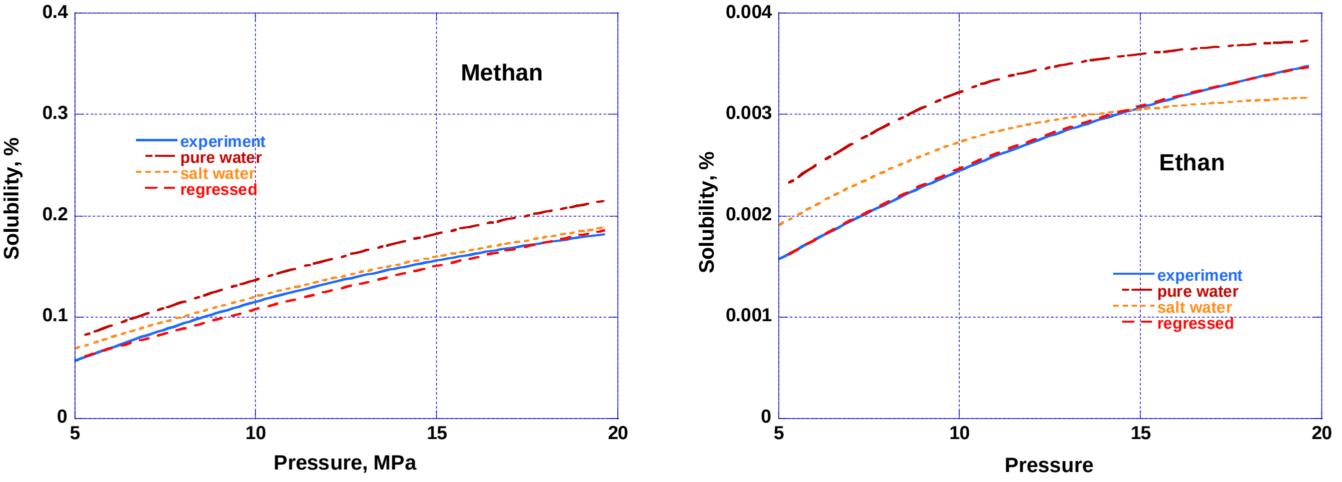

Fig.5 Gas solubility into salt water

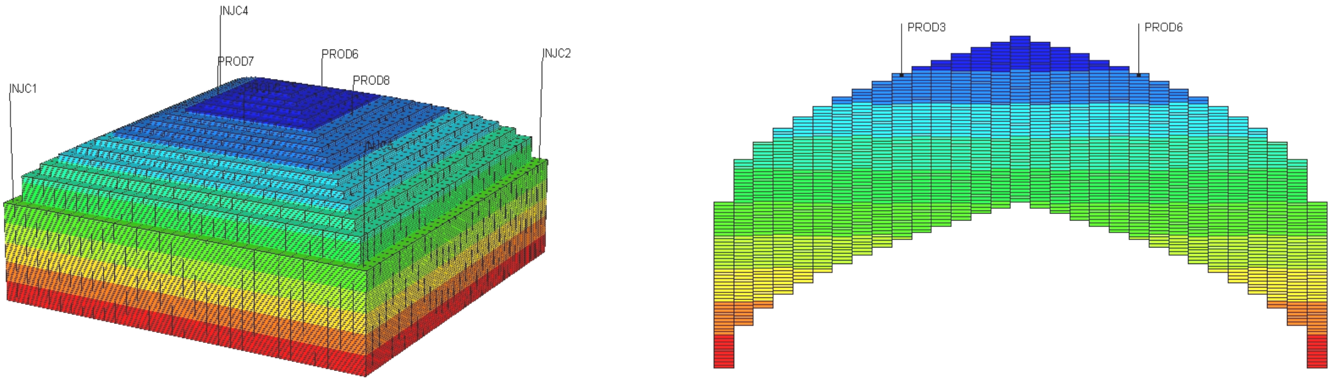

3D view

X-sec

Fig.6 Hypothetical reservoir model (3D and X-sec)

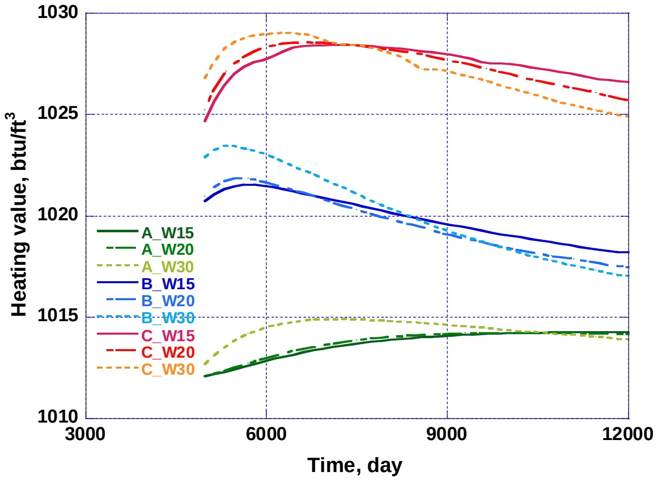

Fig.7 Heating values of withdrawn gases with various in situ fluid composition

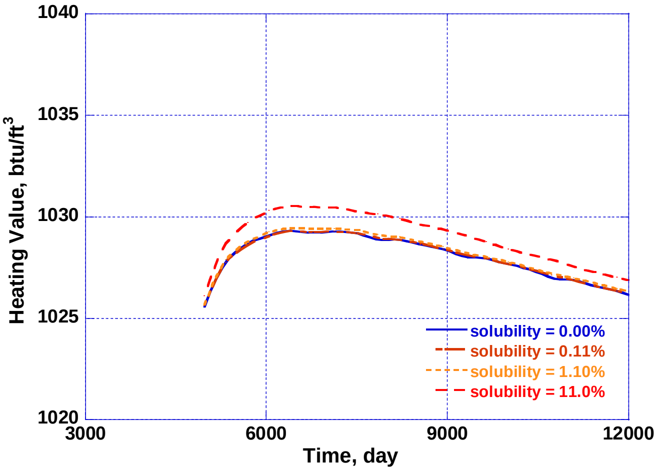

Fig.8 Heating values of withdrawn gases with various methan solubility into water (nitrogen cushion gas volume 20%, working volume 20%)

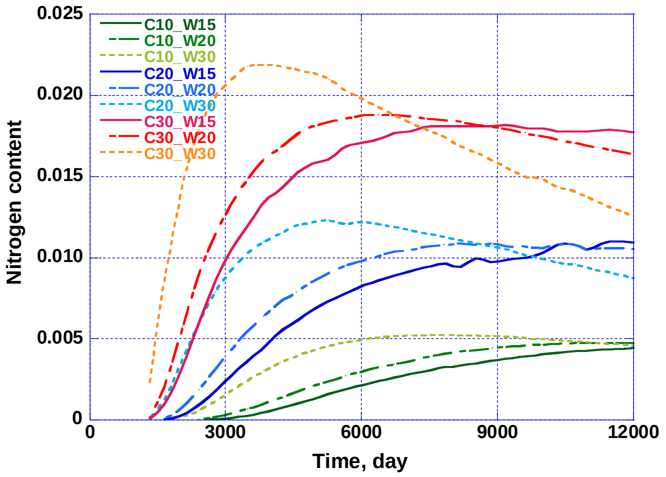

Fig.9 Effluent nitrogen contents with various cushion gas volumes and workinggas volumes

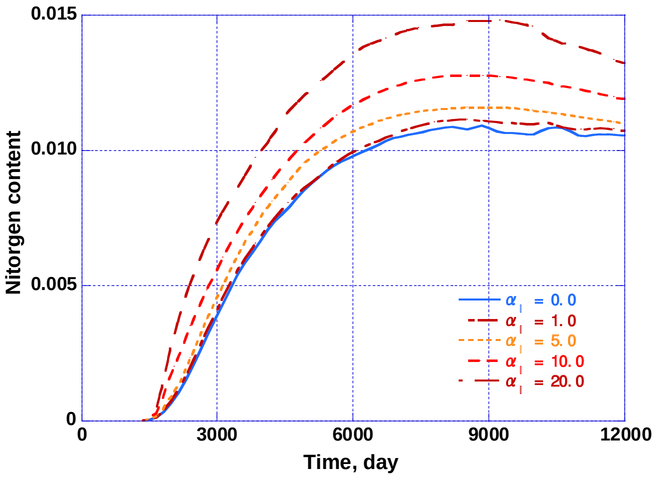

Fig.10 Effluent nitrogen contents with various dispersivities (nitrogen cushion gas volume 20%, working volume 20%)

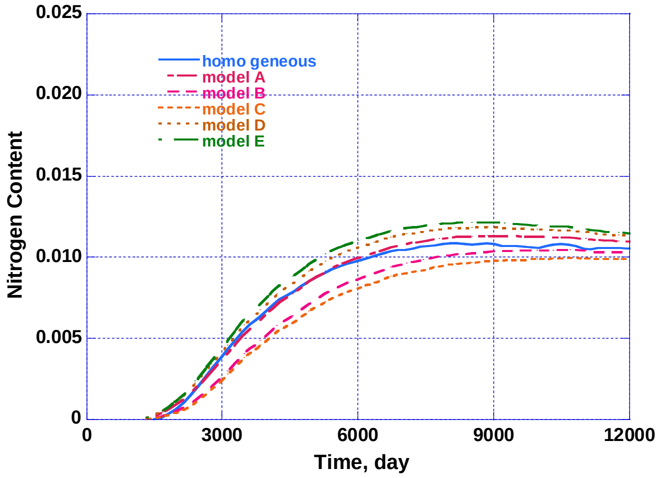

Fig.11 Effluent nitorogen contents with various permeability distributions (nitrogen cushion gas 20%, working volume 20%)

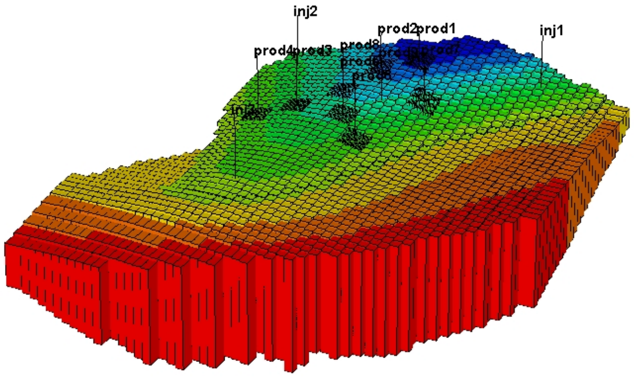

Fig.12 Actual reservoir model (3D view)

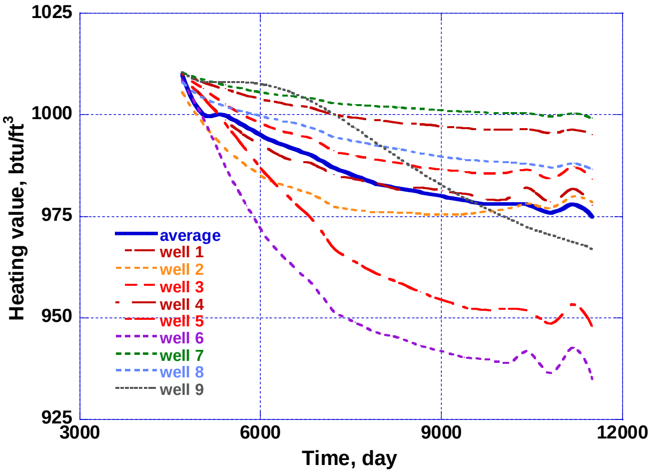

Fig.13 Heating values of withdrawn gases at each well in actual reservoir model